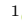



LEONARDO AGUDO JÁCOME<sup>12</sup>, HANS-CHRISTIAN  
HEGE<sup>34</sup>, OLAF PAETSCH<sup>4</sup>, KAI PÖTHKOW<sup>4</sup>

# **Three-Dimensional Reconstruction and Quantification of Dislocation Substructures from Transmission Electron Microscopy Stereo-Pairs**

---

<sup>1</sup>  0000-0001-8839-8815

<sup>2</sup>Bundesanstalt für Materialforschung und –prüfung (BAM), Dept. Materials Technology,  
Unter den Eichen 87, 12205 Berlin, Germany

<sup>3</sup>  0000-0002-6574-0988

<sup>4</sup>Zuse Institute Berlin, Dept. Visual Data Analysis, Takustr. 7, D-14195 Berlin, Germany

Zuse Institute Berlin  
Takustr. 7  
14195 Berlin  
Germany

Telephone: +49 30-84185-0  
Telefax: +49 30-84185-125

E-mail: [bibliothek@zib.de](mailto:bibliothek@zib.de)  
URL: <http://www.zib.de>

ZIB-Report (Print) ISSN 1438-0064  
ZIB-Report (Internet) ISSN 2192-7782

# Three-Dimensional Reconstruction and Quantification of Dislocation Substructures from Transmission Electron Microscopy Stereo-Pairs

Leonardo Agudo Jácome<sup>a,\*</sup>, Kai Pöthkow<sup>b</sup>, Olaf Paetsch<sup>b</sup>, Hans-Christian Hege<sup>b</sup>

<sup>a</sup> *Bundesanstalt für Materialforschung und –prüfung (BAM), Dept. Materials Technology, Unter den Eichen 87, 12205 Berlin, Germany*

<sup>b</sup> *Zuse Institute Berlin, Dept. Visual Data Analysis, Takustraße 7, 14195 Berlin, Germany*

A great amount of material properties is strongly influenced by dislocations, the carriers of plastic deformation. It is therefore paramount to have appropriate tools to quantify dislocation substructures with regard to their features, e.g., dislocation density, Burgers vectors or line direction. While the transmission electron microscope (TEM) has been the most widely-used equipment implemented to investigate dislocations, it usually is limited to the two-dimensional (2D) observation of three-dimensional (3D) structures. We reconstruct, visualize and quantify 3D dislocation substructure models from only two TEM images (stereo-pairs) and assess the results. The reconstruction is based on the manual interactive tracing of filiform objects on both images of the stereo-pair. The reconstruction and quantification method are demonstrated on dark field (DF) scanning (S)TEM micrographs of dislocation substructures imaged under diffraction contrast conditions. For this purpose, thick regions (> 300 nm) of TEM foils are analyzed, which are extracted from a Ni-base superalloy single crystal after high temperature creep deformation. It is shown how the method allows 3D quantification from stereo-pairs in a wide range of tilt conditions, achieving line length and orientation uncertainties of 3 % and 7°, respectively. Parameters that affect the quality of such reconstructions are discussed.

**Keywords:** dislocation, diffraction contrast, scanning transmission electron microscopy, stereoscopy, visualization

## 1. Introduction

The transmission electron microscope (TEM) reproduces two-dimensional (2D) projections of three-dimensional (3D) objects, thus losing information on the spatial arrangement of these objects. Since shortly after the construction of the first TEM, stereo-microscopy has helped to overcome this problem by mimicking the binocular vision of human eyes [1–7]. For this purpose, two micrographs, a so-called stereo-pair, are usually acquired from two differently tilted positions –with a tilt between  $\approx 8^\circ$  and  $20^\circ$ – depicting the same region and then –traditionally– observed as a stereogram in a stereoscope [2]. Alternatively, the 3D impression can be gained by manipulating the digitized stereo-pair such that each eye sees only its corresponding perspective, e.g., by converting the stereo-pair into an anaglyph and observing it with suitably colored filters [e.g. 8].

In order to perform stereo-microscopy on crystalline defects (e.g., dislocations,

\*Corresponding Author: [leonardo.agudo@bam.de](mailto:leonardo.agudo@bam.de)

stacking faults, twins, implanted ions), the images must be acquired by having a common diffraction vector  $\mathbf{g}$  excited at the two tilt settings, such that similar diffraction contrast arises at both perspectives [3]. Stereo-imaging is a suitable method for quantitative measurements of TEM foil thickness [1,3,5,9] and therefore, for determining the dislocation density in crystalline materials [e.g. 10–12]. Furthermore, stereo-microscopy has proved beneficial in determining the line direction  $\mathbf{u}$  and habit plane of dislocations in these material class [e.g. 7,13–15]. Recently, Agudo et al. [8] showed that the use of diffraction contrast in the scanning (S)TEM can significantly improve the quality of stereoscopic methods applied to the 3D characterization of dislocations in thicker regions of strained TEM foils, as compared to the wide spread use of conventional (C)TEM. Major advantages of using diffraction contrast in STEM instead of CTEM are the absence of strong bending contours and through-thickness oscillations [16], thus facilitating a more intuitive 3D impression of stereo-pairs. These differences have been discussed extensively in the past [8,17–24].

Quantities such as dislocation density, dislocation directions and foil thickness are usually measured on stereo-pairs by different manual stereological methods [e.g. 7,25–27], which can be very time consuming. The first and only attempt known by the authors to use TEM stereoscopy to reconstruct dislocation lines, proposed by McCabe et. al [28], discussed the use of weak beam microscopy in single tilt holders. In this setup, only small stereo-angles are applicable on thin regions ( $< 200$  nm) and care must be taken to have useful diffraction conditions, otherwise risking large deviations in the reconstructed depth [28]. For their work, McCabe et. al used Sterecon [29], a system that is similar to the one we implement. Sterecon allows the user to draw contours and curves in 3D using a symmetric stereo-viewing setup. It is a specialized system consisting of both hardware and software, which was developed for segmentation and analysis of image data in biological research. Thanks to the special hardware, the user can navigate in 3D space using a cursor, which is also used for drawing and annotation. In contrast, our system is implemented in the framework Amira, a wide spread general purpose software for analysis and visualization of scientific data [30].

A well-developed alternative –yet elaborate– method for quantitative 3D reconstruction of crystalline defects is electron tomography [31–33]. This technique

requires acquiring many images ( $\geq 60$ ) at short tilt intervals ( $\approx 5^\circ$ ) while keeping the same  $\mathbf{g}$ , and then reconstructing the imaged volume using a tomography algorithm that compiles the information from all the collected 2D images. Strong variations in contrast throughout the tilt series are unavoidable due to, e.g., the increase in effective sample thickness in conventional TEM foils; differences in the excitation error at different tilts; or the excitation of multiple  $\mathbf{g}$  vectors at tilts near low-indexed zone axes. Overcoming these and other effects such as the missing wedge is rather challenging and requires exceptional experimental conditions as well as powerful post-processing algorithms [e.g. 34]. Thus, for the 3D reconstruction of dislocation substructures, stereo-microscopy can easily avoid many of the drawbacks of electron tomography. The aim of the present study is to explore the use of STEM stereo-pairs to facilitate the reconstruction, visualization and quantification of dislocation structures in thicker regions of TEM foils ( $> 300$  nm). Furthermore, it is our objective to assess the accuracy of the generated 3D models and to show the feasibility of estimating dislocation density and other linked quantitative measures, while overall reducing the amount of work necessary to perform these evaluations as compared to previous stereological approaches.

## 2. Methods

### 2.1. Principle of Reconstruction

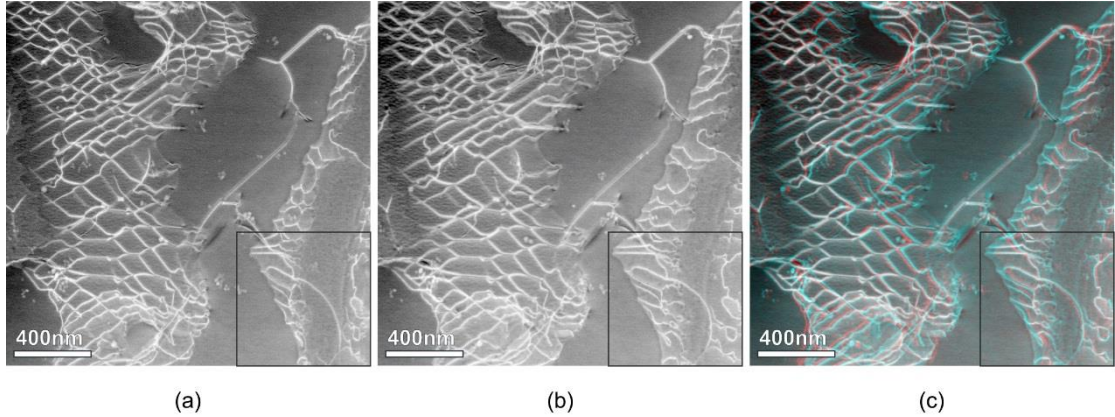
In the proposed reconstruction methods, the depth information  $Z$  in world space is determined on the base of two parameters, granted both images have the same magnification  $M$ . The first parameter is the stereo-angle  $\vartheta$ , tilted along an axis common to the right and left images, which is set to be antiparallel to the world space axis  $\mathbf{Y}$ , and parallel to the vertical edge in both images. The second parameter, which varies with  $\vartheta$ , is the horizontal parallax  $\Delta X$  of an object (point)  $P$ .  $\Delta X$  is defined by points  $P_L$  and  $P_R$  at the respective left and right images, which are the positions onto which a point  $P$  is orthogonally projected at the corresponding tilt positions.

Figure 1 shows a stereo-pair displayed as grayscale images (Figures 1a and b) and as an anaglyph (Figure 1c). The anaglyph in Figure 1c, created from the two images in Figures 1a and b following the procedure by Agudo Jácome et al [8], shows that the features have different relative displacements  $\Delta X$  (see also Figure 5c), which depend on their depth within the TEM foil. This principle is implemented in Section 2.3 in

two methods.

## 2.2. Image Data Setup

Before the actual reconstruction of dislocation structures can be performed by either of the two methods proposed here, the image data must be prepared to be properly aligned in the world space. As a first step, the left and right images of the stereo-pair must be rotated so that their features share the common tilt axis, which, as mentioned in Section 2.1, is then set to be antiparallel to (but not necessarily coincident with) the world space direction  $Y$ . Subsequently, the images must be aligned such that only relative horizontal displacements are present, i.e.,  $\Delta Y = Y_R - Y_L = 0$  for all points  $P$ . This step is taken in both of the presented implementations by only moving the left image in a way that its center is always on the  $XY$  plane. Additionally, the images must be calibrated to world space units. All the images and the resulting graphs shown here are calibrated in nanometers unless otherwise stated.



**Figure 1:** Dislocation structures in a TEM foil of crept Ni-base single crystal superalloy. Left (a) and right (b) grayscale image of a stereo-pair using the same diffraction vector  $\mathbf{g} = (00\bar{2})$  (pointing upwards), and their resulting anaglyph (c). An enlargement of the region marked by black squares is shown in Figures 3 and 5. For further details on the stereo-pair see reference [8].

## 2.3. Two Methods of Reconstruction

In the following, two methods are presented for the reconstruction of 3D dislocation networks from stereo-pairs. Before the reconstruction can take place, the first consideration should be given to the relationship of the coordinate systems associated to real (world) space, to the TEM foil, to the crystal, and to the left and right images. The coordinate systems of the images can be defined in terms of their

respective beam directions  $\mathbf{B}_L$  and  $\mathbf{B}_R$  (assumed here as being orthogonal to and pointing into the respective image plane), the tilt axis direction  $\mathbf{n} = \mathbf{B}_L \times \mathbf{B}_R$  (vertical on both image planes), and the vector products  $\mathbf{T}_L = \mathbf{B}_L \times \mathbf{n}$  and  $\mathbf{T}_R = \mathbf{B}_R \times \mathbf{n}$  (horizontal on the image plane for the left and right image, respectively) [7]. As usual,  $\mathbf{B}_L$  and  $\mathbf{B}_R$  can be determined by indexing the Kikuchi or CBED patterns associated to the tilt positions for the left and right micrographs, respectively. Thus,  $\mathbf{B}$ ,  $\mathbf{n}$  and  $\mathbf{T}$  can be directly expressed in terms of crystallographic directions for samples with cubic symmetry. Additionally, the common stereoscopic experiment in diffraction contrast, where the same diffraction vector  $\mathbf{g}$  is used for both images, yields  $\mathbf{n} = \mathbf{g}$  or  $\mathbf{n} = -\mathbf{g}$ , as in the example shown in Figure 1. In Section 3.3.4, examples where a different diffraction vector is used for each of the two images in the stereo-pair are discussed.

Thus, two main differences between the two reconstruction setups introduced here are noted: 1) the relative tilt of the images with respect to the world coordinate reference, represented by the normalized vectors  $\hat{\mathbf{e}}_X$ ,  $\hat{\mathbf{e}}_Y$  and  $\hat{\mathbf{e}}_Z$ , and 2) the position of the tilt axis for the images with respect to the axes  $X$ ,  $Y$  and  $Z$ .

### 2.3.1 Fully Interactive Method

The “interactive method” receives its name from the fact that it uses a visual interface to manually change the depth of a point  $P$ , previously drawn on the left image at its projected position  $P_L$ , until its projection matches the correct position  $P_R$  on the right image, which is tilted with respect to the left image (see Figure 2).

A schematic representation of the quantities describing the geometry adopted by the setup of the left and right image of the stereo-pair in the implementation of the interactive method is shown in Figure 2. Both, the left and right image are shown edge-on in Figure 2, represented by thick black lines with image centers  $C_L$  and  $C_R$ , respectively. In Figure 2,  $\mathbf{B}$ ,  $\mathbf{n}$  and  $\mathbf{T}$  are shown as unit vectors  $\hat{\mathbf{e}}$  in the coordinate systems drawn on the far-right edges of the left and right image. Note that, for this reconstruction method, the world coordinate system axes, with origin at point  $O$  and represented by the orthonormal system of vectors  $\hat{\mathbf{e}}_X$ ,  $\hat{\mathbf{e}}_Y$  and  $\hat{\mathbf{e}}_Z$ , are set to be parallel (or antiparallel in the case of  $\hat{\mathbf{e}}_Y$ ) to the coordinate system for the left image. The tilt axis passes through point  $O'$  on the  $XY$  plane, so that the right image adopts the tilt  $\theta$  with respect to the left image, as shown in Figure 2.

The observation of point  $P$  in the TEM foil projects it orthogonally onto the left and right images at positions  $P_L$  and  $P_R$ , respectively (see schematic left and right eyes





tracing the dislocations on the left image on its image plane (i.e., connected points  $P_L$ ; see black lines in Figure 3a). By doing this, every point connecting the dislocations already receives its correct  $X$  and  $Y$  coordinate, but still  $Z = 0$ . At this step, the traced network thus appears as a continuous black line on the edge-on view of the left image in Figures 3d and e. By looking orthogonally at the right image plane with the lines traced on the left micrograph projected on top (Figure 3b), it becomes clear that most of the lines do not fall onto their correct positions, e.g., at points projected onto  $1_R$  and  $2_R$ . This effect is due to two reasons. First, the projection of the lines on a plane that is inclined to this perspective, i.e., the traced lines in Figure 3b, appear contracted in  $X$  direction proportional to  $\cos(\vartheta)$  with respect to the black lines in Figure 3a. Second, differences in  $Z$  induce different parallaxes in the white dislocation lines seen in Figure 3b. Only by moving each point along the  $Z$  direction can the projection of each traced point be simultaneously kept on the left micrograph and brought to coincidence with the image features on the right micrograph, as seen in Figure 3c, and consequently to the correct  $Z$  coordinate, as shown in Figure 3f. The latter procedure is thus observed on the right image, e.g., as the displacements of the ends of the dislocations at the respective top and bottom surface points 1 and 2. Care is needed to consider each node individually during this procedure, otherwise risking reconstruction artifacts as described in Section 4.1. The displacements seen on the right image are thus related but not equal to the parallaxes  $\Delta X_1$  and  $\Delta X_2$ , as defined for this method (see Figure 3f).

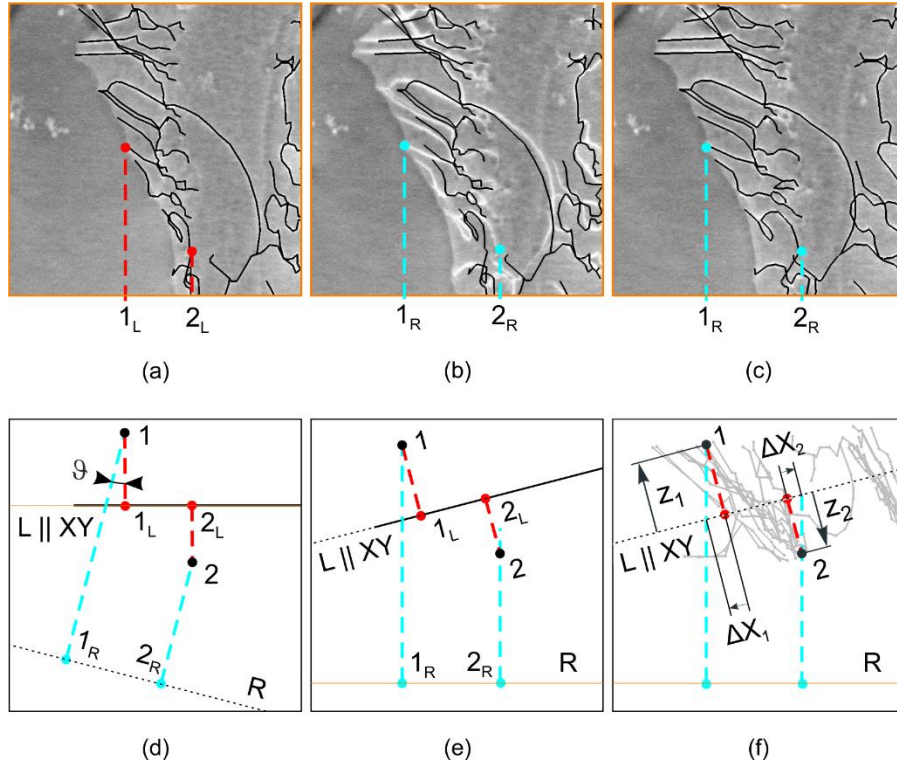


**Figure 3:** Image details of bottom right region in Figure 1 (a-c) and schematic drawings with images of the top row viewed edge-on (d-f), showing the steps taken through the procedure for the interactive reconstruction method. Points 1 and 2, respectively on the top and bottom TEM-foil surface, are exemplarily marked. Black, red and cyan dots respectively mark 3D positions in the foil, on left image and on right image. (a,d) Lines traced on left image (in black). (b,e) Same lines (as traced on left image) viewed on the right image. (c) Correctly overlaid lines on right image achieved by changing the depth  $Z$ , which generates the light gray-colored reconstructed network in (f). For details, see Section 2.3.1.

Thus, a reconstruction by the interactive method is carried out solely by considering the geometrical constraints of stereomicroscopy and matching the  $Z$  coordinate that satisfies the projections on the micrographs under visual control, but without performing calculations. Nonetheless,  $Z$  could also be calculated, as will be described in Section 6. It should be noted that, because this method fixes the transmitted beam direction from the left image  $\mathbf{B}_L$  as being parallel to the world space axis  $Z$ , the resulting foil region is reconstructed as being tilted from the reference plane  $XY$  by the absolute tilt required for the sample, to reach this diffraction condition. This information is important if a coordinate transformation needs to be performed to determine the correct crystallographic line orientations, as will be described in Section 2.4. It is also noted that a shift of the left image along the  $X$

direction would exert an increase  $\Delta X_L$  in horizontal parallax  $\Delta X$  equal to this shift. Consequently, every point  $P$  would also see the same depth shift  $\Delta Z$  in a way that the reconstructed points  $P$  are collectively shifted in space, but without any relative movement between each other.

### 2.3.2 Reconstruction by Independent Vertex Tracing on Both Images

A second approach was tested, in which the reconstruction of the dislocation lines is based on the classical measurement of parallaxes and subsequent calculation of their depth. It is important to be aware that this reconstruction method is only accurate if the sample is tilted symmetrically from the zero-tilt position [5]. The latter is defined as the position where the foil normal would be parallel to  $\mathbf{B}$ , assuming a perfect foil, i.e., with both surfaces parallel to the sample holder axis. This symmetric tilt has taken place in the example given in Figure 1, although it represents rather an exception than the rule in stereoscopic analysis of crystalline defects, where the needed imaging conditions are not necessarily symmetric with respect to the TEM column axis. In this approach, the same feature point (or vertex), e.g., the same end or corner point on a dislocation line, is traced independently on the left and right image. The depth is subsequently computed from the parallax of two vertices denoting the same feature point and the knowledge of  $\vartheta$ , as indicated by the equation above. Thus, we name this method “by vertex”.

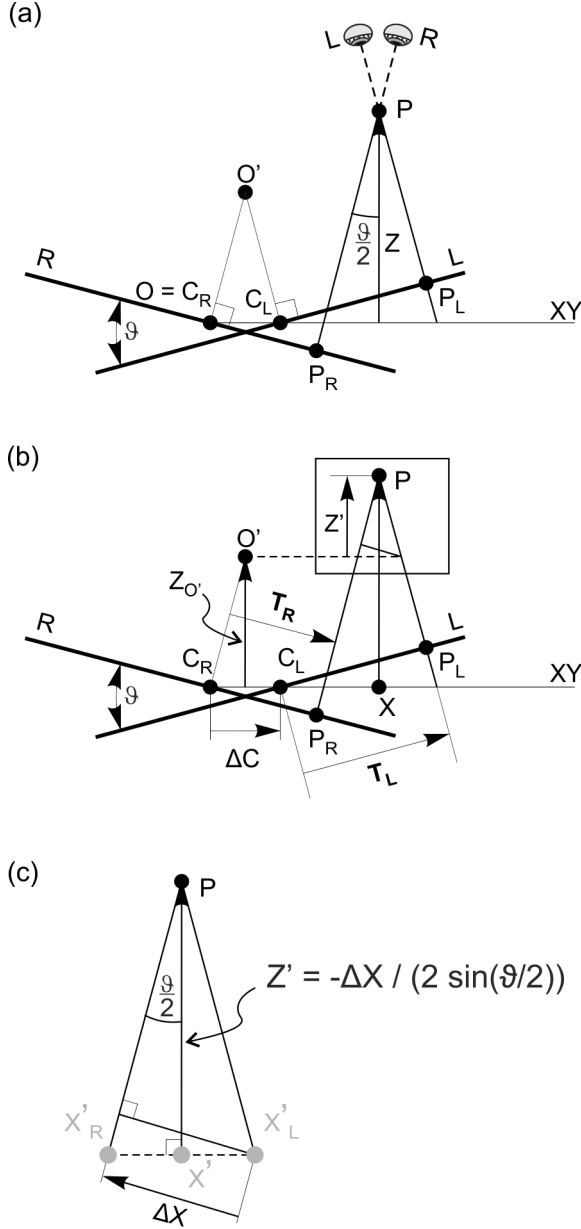


**Figure 4:** Geometric and coordinate relations for the reconstruction using the method by vertex. (a) Relative location of points and planes that define the geometry for determination of  $Z$ . (b) Quantities necessary for calculation of depth coordinate  $Z$ . (c) Enlargement of upper right region in (b), defining traditional parallax equation. See Section 2.3.2 for details.

The geometric relationships defined for the method are shown in Figure 4, which has been divided in three parts for the purpose of clarity and contains features already defined in Figure 2. The images seen by the left and right eyes are again drawn as thick black lines (viewed edge-on), which are marked as  $L$  and  $R$ , respectively. For this method, each of the images assumes opposite tilts around a common axis  $n$  (orthogonal and pointing into the plane of the drawing) that passes through the point  $O'$ . This point is located at the intersection of the lines that are orthogonal to the left

and right image and pass through their respective centers  $C_L$  and  $C_R$ , where the latter point coincides with the world space origin  $O$  (Figure 4a). Figure 4a shows that the left and right images are respectively tilted around  $n$  by  $-9/2$  and by  $9/2$  so that the  $XY$  plane is parallel to the plane bisecting them. Thus, the coordinate  $Z$  for point  $P$  is once more found at the intersection of the lines orthogonally back-projected from points  $P_L$  and  $P_R$  on the left and right image, respectively (Figure 4a).

The interactive method differs from the method by vertex in that for the latter, the parallax  $\Delta X$  is measured and the coordinate  $Z$  then computed based on the traditional parallax equation. Thus,  $Z = Z' + Z_{O'}$ , where  $Z' = -\Delta X / (2M \cdot \sin(9/2))$  (the parallax equation) [6], is here the depth measured from the plane parallel to  $XY$  that passes through the rotation axis at  $O'$  (see dotted line in Figure 4b). The negative sign is due to our definition of  $\Delta X$  (see below).  $M$  (the magnification) is ignored here, as the images are previously calibrated in world units (see Section 2.2). The geometrical construction of the parallax equation that defines  $Z'$  is found at the detail marked by a rectangular region in Figure 4b and enlarged in Figure 4c. The figure shows that only  $\Delta X$  and  $9$  are needed to determine  $Z'$  via two characteristic right triangles that are linked by the segment  $X'_R X'$ . The parallax  $\Delta X = T_R - T_L$  is obtained from the scalar difference between the transversal components  $T_R$  and  $T_L$  of the segments measured from their respective image centers  $C_R$  and  $C_L$  to points  $P_R$  and  $P_L$  (see Figure 4b). It is important to keep the consistency in the signs of  $T_R$  and  $T_L$ , which affects the sign of  $Z'$  (and of  $X$ ). The component  $Z_{O'} = \Delta C / (2 \tan(9/2))$  can be calculated from the known displacement of  $C_L$  from the origin  $O$ ,  $\Delta C$ , on the  $X$  axis (see Figure 4b). A special case is given if  $C_L = C_R$ , so that  $Z = Z'$ . Finally, the coordinate  $X$  of point  $P$  can be computed as  $X = C_R C_L / 2 + O' X'_R + X'_R X'$ , where  $O' X'_R = T_L / \cos(9/2)$  and  $X'_R X' = (-\Delta X / 2) / \cos(9/2)$  (see Figures 4b and c). If  $\Delta X$  is substituted in the latter equation,  $X = \Delta C / 2 + (T_L + T_R) / 2 \cos(9/2)$ .

Analogous to Figure 3, Figure 5 shows the steps taken to reconstruct the lower right region of the stereo-pair in Figure 1 using the method by vertex. The process starts by independently tracing the nodes and lines on both, the left (Figures 5a and e) and right (Figures 5b and f) image, e.g., nodes  $1_L$  and  $2_L$  on the left image plane and nodes  $1_R$  and  $2_R$  on the right image plane. For simplicity, the image centers  $C_L$  and  $C_R$  have been set to coincide so that the origin  $O$  and the location of the tilt axis at  $O'$  also coincide (Figures 5c and g). As the anaglyph in Figure 5c is a construct where both left and right image are merged in the same plane, the parallax can then be directly

measured on it, e.g.,  $\Delta X_1$  and  $\Delta X_2$  on Figures 5c and g. As  $O'$  coincides with  $O$ , i.e., it lies on the  $XY$  plane for the reconstructed example presented in Figures 5d and h,  $Z' = Z$  and the geometric construction for  $Z_1$  and  $Z_2$  in Figure 5h is equivalent to Figure 4c, with the base of the isosceles triangles on the  $XY$  plane. Hence, the parallaxes  $\Delta X_1$  and  $\Delta X_2$  start at the respective intersections between the normals to the left image (red lines) and the  $XY$  trace, and end orthogonally at the normals to the right image (blue lines). Figure 5d thus shows the final position of the reconstructed black lines in the  $XY$  plane, which appear gray on the  $XZ$  view of Figure 5h.

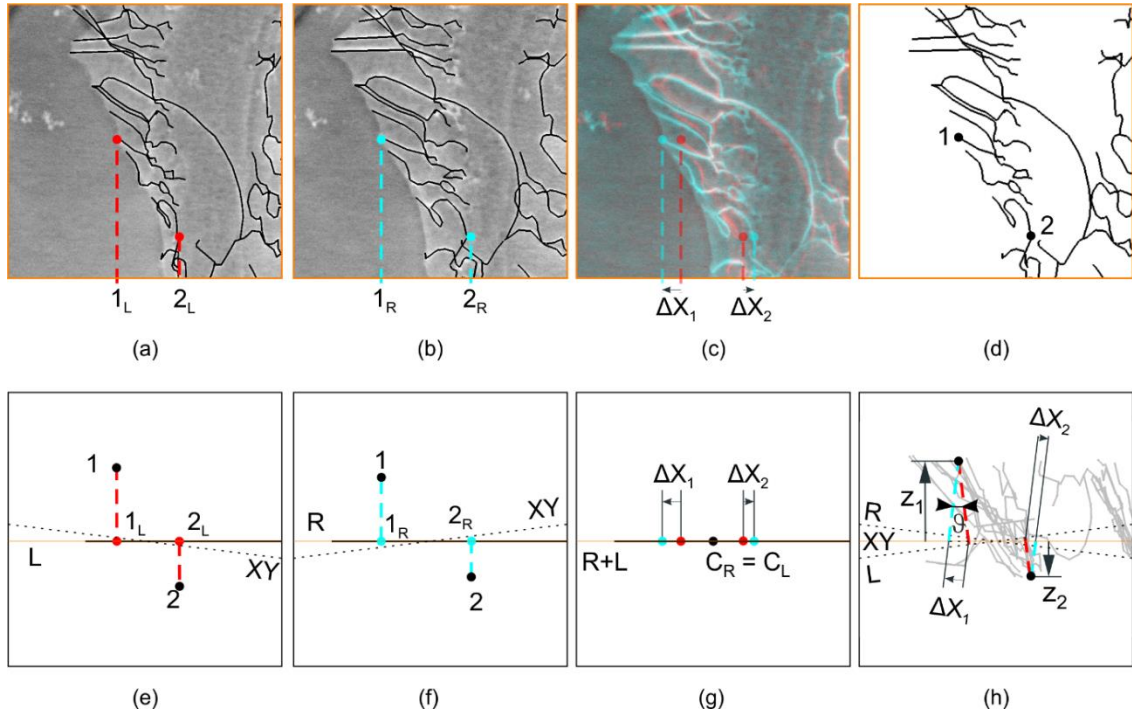


**Figure 5:** Image details of bottom right region in Figure 1 (a-c) resulting top view of the reconstruction (d) and schematic drawings of side views (e-h), showing the steps for the method by vertex. Points 1 and 2 on the top and bottom TEM-foil surface, respectively, are marked with black, red and cyan dots for 3D positions in the foil, on left and on right image, respectively. (a,e) Lines traced on left image (in black). (b,f) Lines independently traced on right image plane. (c,g) Superposition of images and traced objects gives the parallaxes  $\Delta X_1$  and  $\Delta X_2$ , needed together with the stereo-angle  $\vartheta$  to compute  $Z_1$  and  $Z_2$ . The computation is graphically represented in (h). The spatial graph is black in (d), and gray in (h). Black dotted lines mark the reference plane  $XY$  in (e) and (f), and the traces of the left and right image in (h). The plane  $XY$  coincides with the trace of the reconstruction in (h).

## 2.4. Dislocation Line Directions

Together with the Burgers vector  $\mathbf{b}$ , the knowledge of the crystallographic line direction  $\mathbf{u}$  characterizes the dislocation segments, i.e., if it is of screw ( $\mathbf{u} \parallel \mathbf{b}$ ), edge

( $\mathbf{u} \perp \mathbf{b}$ ) or mixed ( $\mathbf{u} \angle \mathbf{b}$ ) character. Often,  $\mathbf{u}$  is determined stereologically on TEM micrographs, e.g., by trace analysis on a tilt series [7]. Thus, obtaining crystallographic line directions from the generated spatial graphs represents an improvement of statistics with respect to manual determination on each segment. Given the nature of stereomicroscopy, the reconstructed volume usually has its crystallographic lattice vectors tilted with respect to the world coordinate system. In order to have the correct indexes for  $\mathbf{u}$ , the crystallographic axes of the reconstructed model must be transformed to meet specific relationships with the space coordinate axes  $\mathbf{X}$ ,  $\mathbf{Y}$  and  $\mathbf{Z}$ . As mentioned in Section 2.3, knowledge of  $\mathbf{B}$ ,  $\mathbf{n}$  and  $\mathbf{T}$  on the corresponding image in terms of crystallographic directions, as well as the image position with respect to the world coordinate axes, allows these crystallographic transformations by using the corresponding transformation matrix [e.g., 37]. In the case of the Ni-Base superalloy data presented here, a convenient transformation consists only in rotating the reconstructed volume in a way such that the lattice vectors of the fcc lattice coincide with the world coordinate system, i.e.,  $[100]_{\text{fcc}} \parallel \mathbf{X}$ ,  $[010]_{\text{fcc}} \parallel \mathbf{Y}$  and  $[001]_{\text{fcc}} \parallel \mathbf{Z}$ .

## 2.5. Software Implementation

The extendable visualization system Amira<sup>1</sup> was used to implement the specific features needed for the methods described here. A specific editor that facilitates the reconstruction and manipulation of thread-like curves and linear structures (the Filament Editor [36]) was extended and adapted to allow the interactive reconstruction of 3D dislocation structures from transmission electron microscopy stereo-pairs. These 3D structures are stored in an Amira-specific data structure called *spatial graph*, consisting of nodes and edges, and data thereon. Furthermore, two modules were added: one to allow a coordinate system transformation into a crystallographic coordinate system; and the other, to compute the depth from two 2D (with Z-component of nodes set to 0) spatial graphs<sup>2</sup>.

---

<sup>1</sup> We use version ZIBAmira2015.40, which for simplicity will be addressed as Amira for the remaining of this paper unless explicitly written.

<sup>2</sup> The extensions to Amira (Linux-binaries and sources) and an example image stereo-pair, together with a tutorial, can be downloaded from <http://www.zib.de/software/STEM-Stereo>

### 3. Experiments and Results

#### 3.1. Material

The German grade Ni-base superalloy single crystal LEK 94 is used throughout the present work to demonstrate the reconstruction and analysis of dislocation networks. Ni-base superalloy single crystals are composed of a two-phase microstructure, where the disordered (fcc)  $\gamma$  phase and the ordered ( $L1_2$ )  $\gamma'$  phase form a coherent interface with a cube-on-cube orientation relationship (see, e.g., Fig. 8b of [37]). During creep deformation, fine regular networks develop at  $\gamma/\gamma'$  interfaces from dislocations that glide in the ductile  $\gamma$  phase. After long-term high temperature creep strain ( $\approx \epsilon_{creep} > 0.005$ ), the two phases develop a wavy shape commonly known as “rafting” and dislocations at the interface networks pair up to jointly penetrate into the  $\gamma'$  phase, a process commonly known as “cutting”. The experimental images were acquired on specimens subjected to tensile creep deformation in  $[100]$  and  $[110]$  at 1293 K and 160 MPa, to a plastic strain  $\epsilon_{creep} = 0.02$ . The details of the experimental conditions and preparation of the samples shown here have been well documented previously [27].

#### 3.2. Transmission Electron Microcopy (TEM)

The micrographs shown here were acquired in STEM mode at an acceleration voltage of 200 kV, using the built-in high angle annular dark field (HAADF) detector in a TECNAI F20 S-Twin. The beam convergence angle was measured as 32.4 mrad and the detector acceptance angle spanned from 22.7 to 113.7 mrad. These parameters were chosen in order to obtain the strongest diffraction contrast. Details on the tilt conditions for the stereo-pairs will be given where needed.

#### 3.3. Evaluation

##### 3.3.1. Foil Thickness, Dislocation Line Lengths and Dislocation Densities

The complete region shown in Figure 1 was reconstructed using the interactive method, the spatial graph of which can be appreciated in Figure 6. With a complete reconstruction, it is possible to quantitatively evaluate data such as dislocation line length, foil thickness and dislocation density. Additionally, the data can help differentiating between dislocations localized at various regions, e.g., at  $\gamma/\gamma'$  interfaces, dislocations still gliding in the  $\gamma$  channels and dislocations cutting through the  $\gamma'$  rafts. The second column in Table 1 lists dislocation line lengths for the



different regions (labeled in first column in Table 1) found in the example given in Figure 6. The foil thickness can easily be measured by knowing features located at the upper and lower foil surfaces of the foil, e.g., dislocation endpoints 1 and 2. This is illustrated in Figure 7, where the foil region reconstructed in Figure 6 is now viewed edge-on and a local foil thickness  $t \approx 370$  nm is measured. Although common  $\mathbf{g}$  was selected for the stereo-pair in Figure 1, such that as many dislocations as possible would be visible, please note that the dislocation line lengths and densities in Table 1 underestimate the real values because some segments are effectively invisible and thus are not traced, i.e., the Burgers vector  $\mathbf{b}$  of these segments is directed in such a way that it does not give rise to contrast for the chosen  $\mathbf{g}$  [e.g., 6].

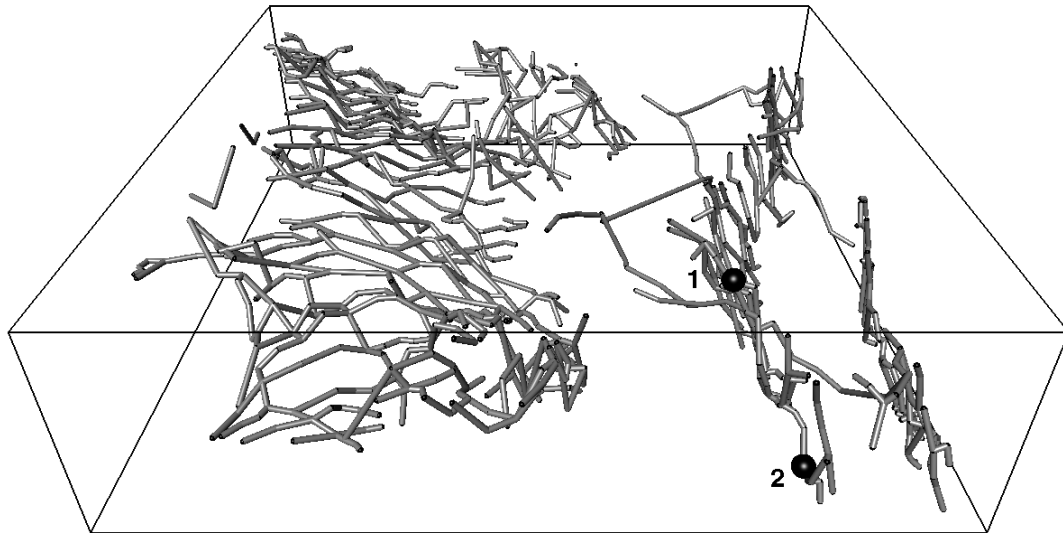


**Figure 6:** Perspective view of reconstructed full region shown in Figure 1. Points 1 and 2 (see Section 2.3) are marked as black dots.

**Table 1:** Dislocation line lengths and densities (referred to evaluated volume in Figure 6) from different characteristic regions in rafted structure of crept Ni-base superalloy single crystal.

Region	Dislocation line length (nm)	Dislocation density ( $10^{12} \text{ m} \cdot \text{m}^{-3}$ )
$\gamma$ channels	2,423	1.7
$\gamma'$ rafts	3,802	2.7
$\gamma/\gamma'$ interface	57,342	40.0

In principle, the method can be equally employed on stereo-pairs of a different

nature, such as dislocation substructures in CTEM diffraction contrast. However, the bending effects of highly deformed samples could hinder proper recognition of the same dislocation line on both images of a stereo-pair [8]. In a similar way, shapes other than lines could also be quantified, e.g., the depth position of round particles, the length of lath-shaped precipitates or even plate-like shapes with well-defined in-plane boundary directions.

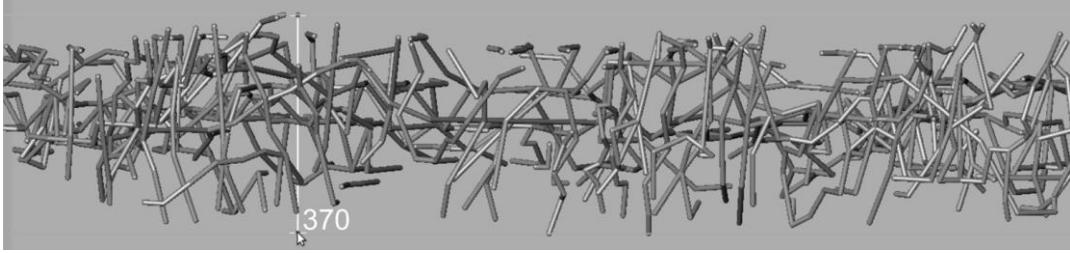


**Figure 7:** Example of a measured foil thickness in an Amira viewer employing orthographic projection on the reconstructed volume of Figure 6.

### 3.3.2. Accuracy Limits in the Ideal Case

In order to evaluate the accuracy of the implemented methods themselves after reconstruction and rotation, we reconstructed a synthetically generated cube lattice, which has the crystal orientations measured for the example given in Figure 1. For this purpose, the Kikuchi line diffraction patterns (KLPs) associated to the left and right tilt positions in Figures 1a and b, respectively (see Figure 4a of [8]), were evaluated to: 1) generate the projections of the unit cubic lattice associated to the stereo-pair, following the procedure by Dlouhý & Eggeler [1–7]; 2) reconstruct the 3D cubic lattice by the two methods described in Section 2.3; and 3) rotate the data to match the crystal and world coordinate systems, as explained in Section 2.4. The images for the reconstruction were scaled to have a pixel size of 0.1 nm and show a cube length of 100 nm. The cube in the left of Figure 8 was reconstructed by the interactive procedure, whereas the procedure by vertex was implemented for the cube on the right. Although both reconstructions present  $\langle 100 \rangle$ ,  $\langle 110 \rangle$  and  $\langle 111 \rangle$  lines, only the sides and face diagonals of a square can be seen on both spatial graphs, while the remaining segments are underlaid behind these lines and the vertices that join them. Several attributes of each  $\langle 100 \rangle$  line displayed in Figure 8 are listed in Tables 2 and 3 for the cubes reconstructed interactively and by vertex, respectively. The attributes listed include the line identification number (ID), Miller indices ( $u \ v \ w$ ), line length ( $L$ ) and orientation. The latter is listed in both spherical ( $\theta, \varphi$ ) and Cartesian

coordinates ( $X, Y, Z$ ).

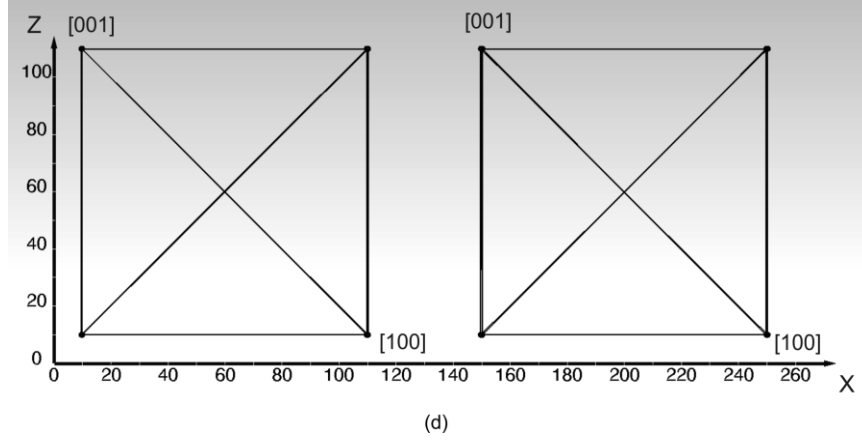


Figure 8: Spatial graphs of lattice cubes reconstructed interactively (left) and by vertex (right) and projected along the world coordinate  $Y$  after crystal reference rotation to match the world coordinate system. Directions  $Y \parallel [010]$ , not labeled, point into the image plane.

**Table 2:** List of attributes of  $\langle 100 \rangle$  lines under idealized image conditions after interactive reconstruction and rotation of lattice cell cube on the left of Figure 8: ID – identification; Miller indices  $[u \ v \ w]$ ;  $L$  – length;  $\theta$  – polar angle;  $\varphi$  – azimuthal angle;  $X, Y$  and  $Z$  – normalized Cartesian coordinates.

ID	$[u \ v \ w]$	$L$ [nm]	$\theta$ [°]	$\varphi$ [°]	$X$	$Y$	$Z$
1	$[1 \ 0 \ 0]$	100.5	90.0	360.0	1.000	-0.001	0.000
2	$[1 \ 0 \ 0]$	100.5	90.0	360.0	1.000	-0.001	0.000
3	$[1 \ 0 \ 0]$	99.8	90.0	0.0	1.000	0.000	0.000
4	$[\bar{1} \ 0 \ 0]$	99.8	90.0	180.0	-1.000	0.000	0.000
5	$[0 \ 1 \ 0]$	100.0	90.0	89.8	0.003	1.000	0.000
6	$[0 \ 1 \ 0]$	100.1	90.0	90.3	-0.005	1.000	0.000
7	$[0 \ 1 \ 0]$	100.0	90.0	89.8	0.003	1.000	0.000
8	$[0 \ \bar{1} \ 0]$	100.1	90.0	270.3	0.005	-1.000	0.000
9	$[0 \ 0 \ 1]$	99.9	0.0	113.2	0.000	0.000	1.000
10	$[0 \ 0 \ 1]$	99.9	0.0	243.4	0.000	0.000	1.000
11	$[0 \ 0 \ 1]$	99.9	0.0	108.4	0.000	0.000	1.000
12	$[0 \ 0 \ 1]$	99.9	0.0	273.8	0.000	0.000	1.000

**Table 3:** List of attributes of  $\langle 100 \rangle$  lines under idealized image conditions after reconstruction by vertex and rotation of lattice cell cube on the right of Figure 8: ID – identification; Miller indices  $[u \ v \ w]$ ;  $L$  – length;  $\theta$  – polar angle;  $\varphi$  – azimuthal angle;  $X, Y$  and  $Z$  – normalized Cartesian coordinates.

ID	$[u \ v \ w]$	$L$ [nm]	$\theta$ [°]	$\varphi$ [°]	$X$	$Y$	$Z$
1	$[1 \ 0 \ 0]$	100.1	89.6	360.0	1.000	0.000	0.008
2	$[1 \ 0 \ 0]$	100.0	90.0	0.0	1.000	0.000	0.000
3	$[1 \ 0 \ 0]$	100.0	90.0	360.0	1.000	0.000	0.000

4	[1 0 0]	100.1	89.6	0.0	1.000	0.000	0.008
5	[0 1 0]	99.9	90.0	90.0	0.000	1.000	0.000
6	[0 $\bar{1}$ 0]	99.9	90.0	270.0	0.000	-1.000	0.000
7	[0 1 0]	99.9	90.0	90.0	0.000	1.000	0.000
8	[0 $\bar{1}$ 0]	99.9	90.0	270.0	0.000	-1.000	0.000
9	[0 0 1]	100.5	0.1	180.0	-0.002	0.000	1.000
10	[0 0 1]	100.5	0.1	180.0	-0.002	0.000	1.000
11	[0 0 1]	99.8	0.2	180.0	-0.003	0.000	1.000
12	[0 0 1]	99.8	0.2	180.0	-0.003	0.000	1.000

The values in Table 2 show that, under idealized imaging conditions, as for stereo-pairs reconstructed in Figure 8 (pixel size = 0.1 nm/pix, line width = 0.1 nm, line length/width ratio = 1000), angular tolerances of  $0.3^\circ$  and length tolerances of 0.5 nm could be achieved from the interactive reconstruction method. Note that the  $\varphi$  values for  $\pm[001]$  vary strongly, depending on the direction towards which the exact orientation deviates, and not on how large this deviation is. Note also that the largest orientation errors, although still small, are found in the  $X$  component of  $\pm[010]$  lines. The largest length errors are seen in  $\pm[100]$  lines. The latter was originally the component with the shortest line projections (see Figure 4b in [8]), due to the short tilt of  $7.25^\circ$ , i.e., the stereo-half-angle  $\vartheta/2$ , from the exact  $[100]$  pole (see Figure 4a in [8]). Small stereo-angles cause the parallax to be also reduced, inducing a large uncertainty in the depth determination for small variations in the parallax measurement. The larger scatter observed for the  $X$  component in  $\pm[010]$  lines could be associated to this condition, as one visually shifts the point on the tilting plane (001) (with  $\mathbf{n} = \mathbf{g}$ ) by finite increments. As a consequence, the deviations in length seen by  $\pm[100]$  lines are accompanied by deviations in orientation on  $\pm[010]$  lines, both families being in the tilting plane.

Table 3 shows equivalent values of line lengths and directions, in this case for the reconstruction by vertex (right cube in Figure 8). For this method, similar angular and spatial tolerances of  $0.4^\circ$  and 0.5 nm, respectively, are achieved. It must be stressed that this comparison is only valid because the stereo-pair in Figure 1 was recorded for a symmetric tilt  $\pm \vartheta/2$  with respect to the zero-tilt position of the foil in the TEM (with a measured asymmetry  $\Delta = 0.32^\circ$ ). Different to the interactive method, the larger errors are not found for  $[001]$  lines. Thus, the independent positioning of vertices on both images could help eliminating the risk of shifting by finite step values, although it is still associated with a certain human error.

### 3.3.3. Parameters Affecting Accuracy of Experimental Reconstructions

The images for the reconstruction in Figure 8 were idealized: the projected lattices were simulated using the crystallographic information from the indexed KLPs; their vertical parallax  $\Delta Y$  needed no manual compensation; it was not needed to cancel their mutual rotation manually (in order to satisfy the condition  $\mathbf{n} \parallel -\mathbf{Y}$ ); all the lines are known to be straight and their projected position is also previously known; the calibration of the line width was chosen to achieve a large line length / width ratio (= 1000); and the images do not suffer from any distortion or lack of focus. Thus, the errors introduced during the lattice cube reconstruction of Figure 8 depended only on the accuracy of the manual positioning of the nodes that join them. Unlike simulated images, the reconstruction of experimental images may suffer further inaccuracies, which could increase the uncertainty of manual tracing and reconstruction. In the following, we list several parameters associated with TEM stereo-pairs, which must be considered:

*Inappropriate stereo-angle:* as stated in Section 2.1, the depth measurement  $Z$  is sensitive to the relative displacement between images  $\Delta X$ , the magnification  $M$  and the stereo-angle  $\vartheta$ . Stereo-pairs have historically been acquired for simultaneous observation of the two projected images by human eyes in the form of stereograms, for which  $\vartheta$  must be chosen in a suitable range. This range is determined by the geometrical constraints of the separation between the left and right eyes, and their distance to the objects being observed. Thus, for a comfortable stereoscopic observation  $\vartheta$  must be smaller than  $\approx 22^\circ$  (depending on the observant and depth differences). However, for such small values of  $\vartheta$ ,  $\Delta X$  will also be small. The accuracy of the measurement of  $\Delta X$  (see Figure 1c) should hence increase proportionally with  $\vartheta$ , so that a more accurate reconstruction may result at the expense of not having a stereogram to observe.

*Wide dislocation lines:* the width of dislocation lines is determined by factors such as the beam convergence angle  $2\alpha$ , the diffraction vector  $\mathbf{g}$  (for a given Burgers vector  $\mathbf{b}$  and line direction  $\mathbf{u}$ ), defocus, spot size, spherical aberration, etc. The aspect ratio (length / width) of short dislocation segments will increase the uncertainty with which the dislocation line can be traced with increasing segment width or decreasing length. A common segment width is  $\approx 4$  nm, as for the images presented here. Therefore, special care must be taken when interpreting line directions of short dislocation

segments.

*Non-proportional scanning distortions:* distortions in scanning images may arise from different sources, e.g., short pixel dwell times, image drift, deflection coil disparities, spherical aberration, etc. Attention must be paid to compensate for distortion sources where possible. If the micrographs must be rotated after image acquisition, these distortions could introduce a varying vertical displacement  $\Delta Y$  in the stereo-pairs, which will hinder matching points for parallax ( $\Delta Y$ ) determination. Horizontal distortions will furthermore cause an inaccurate measurement of  $\Delta X$ .

*Imprecise account of image rotations:* an accurate determination of the relative rotation between images from diffraction and imaging modes is paramount to guarantee the correct determination of the parallax (see Section 2.2). The relative rotation between image and diffraction mode is traditionally measured with reference to CTEM mode. This relative rotation must be measured independently in the STEM mode, even if the same nominal camera lengths and magnifications are stated as for CTEM mode. Fortunately, because STEM is conducted in diffraction mode, the KLPs and the STEM image can be simultaneously observed, allowing the relative rotation between STEM imaging and the diffraction patterns to be checked “online”. Eventually, the STEM mode also offers the possibility to cancel the relative rotation via scan rotation before image acquisition, although this feature might not be sufficiently accurate.

*Curved lines and superimposed lines close to tilt plane:* curved dislocations render the exact placement of their defining vertex points on both images difficult. If they additionally are contained in the tilt plane, the correct trace of points in both images may be impossible from only two images. A third image of the same dislocation line, taken with a different diffraction vector could help identify the shape of the dislocation to trace it properly.

*Loss of focus in effectively thick regions:* this can occur due to chromatic aberration in non-energy filtered CTEM images or in STEM images of strongly tilted samples without dynamical focus correction [8]. Dynamical focus correction of this kind of images will slightly distort it, but the extent of this distortion will usually produce deviations smaller than those from other sources mentioned above. For effective thicknesses, much larger than the depth of field, even dynamical focus will

not work for regions falling out of the latter, giving an experimental limit to the possible foil thicknesses to be investigated with high accuracy.

#### 3.3.4. Quantification of Accuracy

In order to have an idea of how the aforementioned parameters may affect the quantities measured, we compare reconstructions made from stereo-pairs with different tilt conditions by using our interactive method –because it is independent of tilt position, unlike the method by vertex– and two independent stereological methods. For this purpose, the DFSTEM images in Figure 9 were employed to form stereo-pairs that differ in various experimental parameters. Figure 9 shows a tilt series of a region found in a specimen loaded in [001]. The images in Figures 9a to g were acquired under two-beam conditions, as indicated by the inset diffraction vector  $\mathbf{g}$  (thick white arrows). Additionally, a cube lattice showing the corresponding crystallographic tilt has been created for each image in Figure 9, following the work by Dlouhý and Eggeler [7]. The rotation vector  $\mathbf{n}_{1,2}$  has also been marked on each micrograph, where the subindices 1 and 2 refer to the image identification within Figure 8. For example,  $\mathbf{g}$  and  $\mathbf{n}$  coincide for the image pairs 9a,b and 9c,d, as these images form usual stereo-pairs for stereoscopic observation with a common  $\mathbf{g}$ . The different stereo-pairs have been marked by joining their individual micrographs in Figure 9 with a thick black line. In order to perform the reconstruction from pairs with different  $\mathbf{g}$ s, it was necessary to rotate each image in such a way that  $\mathbf{n} \parallel -\mathbf{Y}$ . Table 4 lists all the stereo-pairs and their parameters, including each  $\mathbf{g}$ ,  $\mathbf{B}$  and the absolute foil tilt angle for each micrograph, as well as the tilt plane normal  $\mathbf{n}_{1,2}$  and the stereo-angle  $\vartheta_{1,2}$  formed between the two  $\mathbf{B}$ s.

Figure 9h shows a micrograph acquired in a multi-beam condition with  $\mathbf{B} \parallel [001]$ , which is also close to the foil normal. The superdislocation in the middle of the images in Figure 9 has a Burgers vector  $\mathbf{b} = a[010]$ , where  $a$  is the lattice parameter of the  $\gamma'$  phase. The three main segments of the superdislocation have been labeled 1, 2 and 3 in Figures 9f to h. The aforementioned  $\mathbf{b}$  is the result of having two superpartials with Burgers vectors  $a/2[011]$  and  $a/2[01\bar{1}]$ , so that there is always at least one superpartial visible in every micrograph of Figure 9. Even in Figure 9a, where  $\mathbf{g} \cdot \mathbf{b} = 0$ , all segments exhibit residual contrast, being of mixed character. Additionally, it can be seen on all micrographs in Figure 9 that the long superdislocation segments are straight, oblique between each other and in the length

range 100–300 nm. Figure 10a shows the spatial graphs for the three aforementioned superdislocation segments, generated by interactive reconstruction of the stereo-pairs listed in Table 4. The micrograph pairs used for the reconstructions in Figure 10a are identified in the legend by their labels in Figure 9. By inspecting the segments and the cube direction projections in the tilt series of Figure 9 and from Figure 10a, it seems clear that the three segments are oriented close to different  $\langle 110 \rangle$ . The possible deviations between spatial graphs from different stereo-pairs arise from variables such as those described in Section 3.3.3, and will now be quantified.

In the insets of Figures 9f to h, which show enlargements of the superdislocation in their respective micrographs, one can see that always two of the three segments seem coplanar: segments 2 and 3 appear coplanar in Figure 9f; 1 and 2, in Figure 9g; 1 and 3, in Figure 9h. The three planes containing each segment are thus parallel to respective  $\mathbf{Bs}$  in Figures 9f to h and deviate  $\approx 4^\circ$  off the traces of planes  $(1\bar{1}1)$ ,  $(\bar{1}11)$  and  $(010)$  (see insets in Figures 9f, g and h). As each of the three superdislocation segments is contained in two of these planes, the three segment line directions  $\mathbf{u}_1$ ,  $\mathbf{u}_2$  and  $\mathbf{u}_3$  can be determined via cross product of the corresponding plane normals. This trace analysis gives thus a first independent measure of the three line orientations. We also used the stereological method proposed by Dlouhý & Eggeler [7] as a second independent method to evaluate the line directions and lengths for  $\mathbf{u}_1$ ,  $\mathbf{u}_2$  and  $\mathbf{u}_3$ . They called this quantitative method “analytical”, as opposed to their qualitative “cube projection” method (also implemented in Figures 9a to h). We thus evaluate the same stereo-pairs shown in Figure 9a through e and listed in Table 4, and compare the results with our reconstruction method. The resulting segment line directions from the analytical and interactive methods are plotted in Figure 10b. Filled symbols mark results from our interactive reconstruction method, whereas empty symbols show the results from the analytical method. In Figure 10c only the data points from the interactive method are presented, and compared to the line directions obtained by trace analysis. Three gray-filled circles represent the arithmetic mean from all data points obtained by the interactive method, whereas three white circles show the line directions determined by trace analysis. The orientation deviations of the three segments from the planes  $(1\bar{1}1)$ ,  $(\bar{1}11)$  and  $(010)$  are made graphically clear by drawing their traces on Figure 10c. In Figures 10b and c, line directions are represented as pole figures on the  $(001)$  stereographic projection on a Wulff net with



great circles at  $10^\circ$  intervals. Except for data points from stereo-pairs a,b and c,d for  $\mathbf{u}_2$ , all orientations plotted fall on the northern hemisphere.

**Table 4:** Stereo-pair conditions for images in Figure 9: figure pair label, diffraction vector  $\mathbf{g}$ , beam direction  $\mathbf{B}$ , absolute stage tilts, rotation plane normal  $\mathbf{n}$  and stereo-angles  $\vartheta$ .

pair	$\mathbf{g}_1$	$\mathbf{g}_2$	$\mathbf{B}_1$	$\mathbf{B}_2$	tilt <sub>1</sub> [°]	tilt <sub>2</sub> [°]	$\mathbf{n}_{1,2}$	$\vartheta_{1,2}$ [°]
a,b	(2 0 0)	(2 0 0)	[ 0 15 100]	[ 0 $\bar{14}$ 100]	7.1	7.9	( 1 0 0)	16.3
c,d	(1 1 1)	(1 1 1)	[ $\bar{62}$ $\bar{15}$ 77]	[ $\bar{50}$ $\bar{31}$ 81]	39.0	36.4	( 1 1 1)	11.9
d,f	(1 1 1)	(1 $\bar{1}$ 1)	[ $\bar{50}$ $\bar{31}$ 81]	[ $\bar{49}$ 32 81]	36.4	35.0	( $\bar{85}$ 1 $\bar{52}$ )	36.8
e,g	(1 1 $\bar{1}$ )	( $\bar{1}$ 1 1)	[50 32 81]	[49 $\bar{32}$ 81]	36.7	38.5	(85 0 $\bar{52}$ )	36.9
c,e	(1 1 $\bar{1}$ )	(1 1 1)	[50 32 81]	[ $\bar{62}$ $\bar{15}$ 77]	36.7	39.0	(38 $\bar{92}$ 13)	74.4

Subscripts 1 and 2 refer to first and second micrograph in the stereo-pair, respectively.

The plot in Figure 10d shows the different line lengths obtained for the three superdislocation segments, depending on stereo-pair and applied method. The same geometrical symbols have been used as in Figure 10b, in order to distinguish results from the analytical (open symbols) and interactive (filled symbols) methods.

As mentioned above, it is clear from Figure 10a that all measurements fall around [101] (for  $\mathbf{u}_1$ ), [110] (for  $\mathbf{u}_2$ ) and [ $\bar{1}$ 01] (for  $\mathbf{u}_3$ ). A comparison between the orientation points from the analytical and interactive reconstruction method shows that the reconstruction has a comparable or even better accuracy. Table 5 displays a quantitative account of the accuracy for both methods, considering measurements from all five stereo-pairs given in Table 4 and Figure 9. The mean angular difference in Table 5 refers to the average deviation between the mean orientation determined by a method and its individually determined orientations. The next column in Table 5 gives the maximum deviation measured between the mean orientation within a method and the five individual measurements. The angular spread in the third column of Table 5 is the maximum angle between any two data points for a given segment, thus expressing the accuracy for any single stereo-pair of the region. It can be seen from Figure 10b and Table 5 that the reconstruction consistently shows a better precision than the analytical method. Regarding  $\mathbf{u}_1$  and  $\mathbf{u}_2$ , the larger uncertainty for the analytical method can be partly explained by the outlying data point c,d ( $\angle$ , see arrows in Figure 9b). The data point c,d comes from the stereo-pair with the shortest stereo-angle (Table 4,  $\vartheta_{c,d} = 11.9^\circ$ ), which increases the probability of inaccurate

orientation determination, as explained in Section 3.3.3.

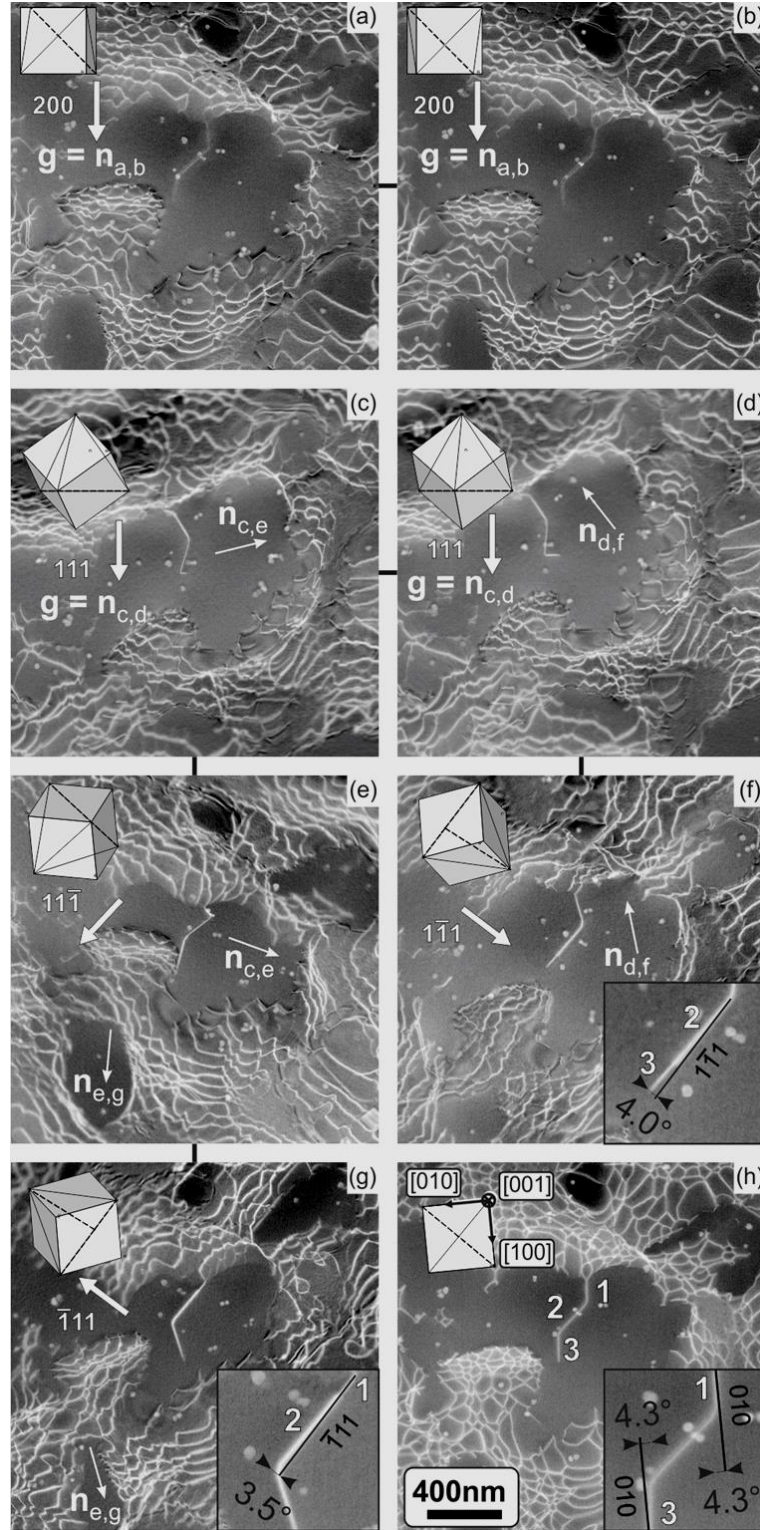
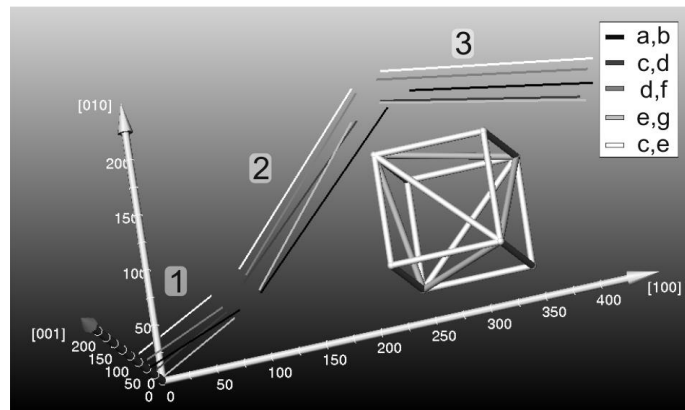
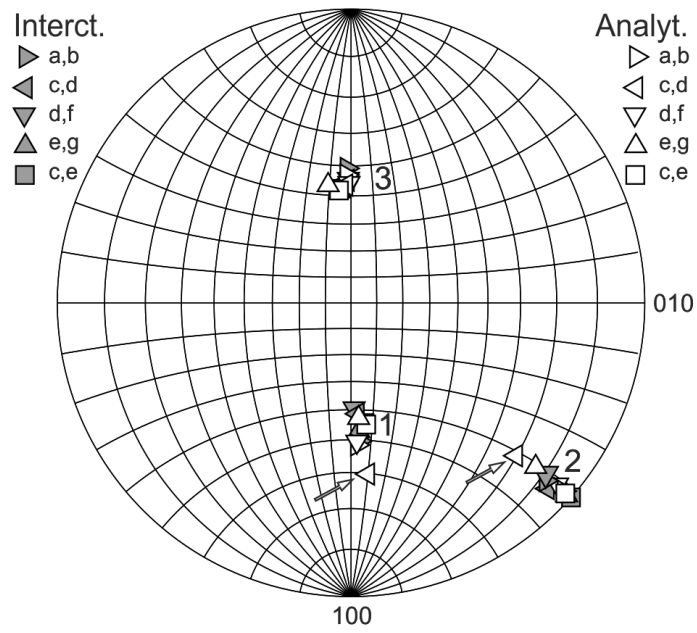


**Figure 9:** Tilt series of a region in a specimen loaded in  $[001]$ , with a foil normal  $\approx [00\bar{1}]$ . An inset lattice cube shows the crystallographic tilt in each micrograph. DFSTEM micrographs under different two-beam conditions: (a)  $g$  (200); (b)  $g$  (200); (c)  $g$  (111); (d)  $g$  (111); (e)  $g$  ( $11\bar{1}$ ); (f)  $g$  ( $1\bar{1}1$ ); (g)  $g$  ( $\bar{1}11$ ). The vectors  $n$  are shared with micrograph pairs of the series. In (h), taken under a multi-beam condition ( $B = [001]$ ), three straight segments of the central superdislocation are labeled. Insets (bottom right) in (f), (g) and (h) show a magnification of the superdislocation. See text for details.



(a)



(b)

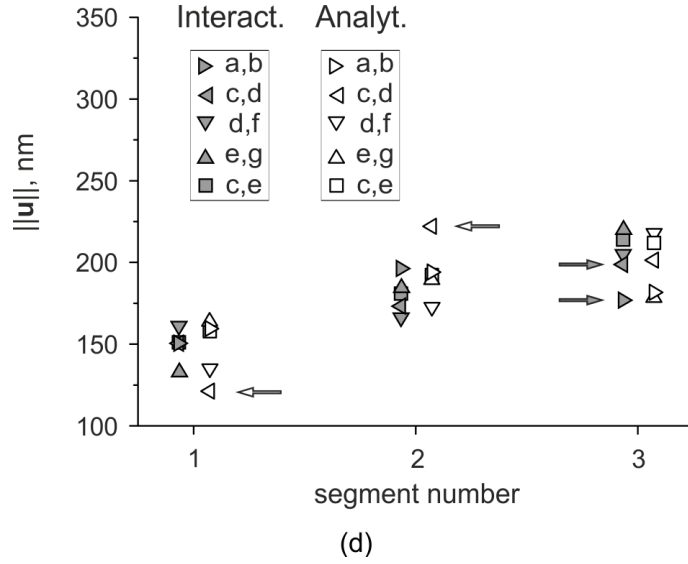
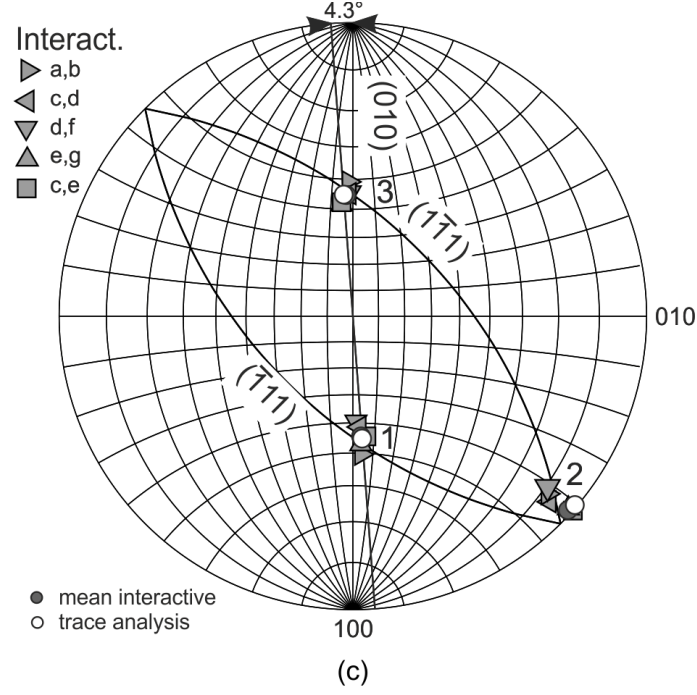


**Figure 10:** Evaluation of superdislocation segments 1, 2 and 3 from Figure 9. (a) Spatial graphs from five stereo-pairs (for an anaglyph, see Figure 4 of [39]). Axis units in nm. (b) Stereographic projections for  $\mathbf{u}_1$ ,  $\mathbf{u}_2$  and  $\mathbf{u}_3$  obtained by analytical [7] (empty symbols) and interactive (filled symbols) method. (c) Stereographic projections for  $\mathbf{u}_1$ ,  $\mathbf{u}_2$  and  $\mathbf{u}_3$  obtained by trace analysis (empty circles) and interactive (filled symbols) method. (d) Plots of line lengths  $\|\mathbf{u}_1\|$ ,  $\|\mathbf{u}_2\|$  and  $\|\mathbf{u}_3\|$  for analytical (empty symbols) and interactive (filled symbols) method. See Section 3.3.4 for details.

The presented values on the accuracy of the reconstruction method are not as strongly affected by the data point c,d, albeit this fact is due to a more robust method or it is a mere coincidence for both,  $\mathbf{u}_1$  and  $\mathbf{u}_2$ . The stereo-pair a,b also shows a low stereo-angle ( $\vartheta_{a,b} = 16.3^\circ$ ) because both of these stereo-pairs were originally acquired for stereoscopic observation. On the other hand, the simultaneous observation of an

anaglyph during tracing can be very convenient. Without it, manual matching of lines could become a demanding job in regions with large dislocation densities, as the stereo-angle increases and relative displacements between lines become difficult to follow.

Taking the latter factor into account, Table 6 shows the mean angular difference, the maximum deviation from the mean and the absolute angular spread from the data points shown in Figure 10b, excluding the measurements for stereo-pairs a,b and c,d. From Table 6 it becomes clear that a larger stereo-angle ( $37^\circ < \vartheta < 75^\circ$ ) improves the accuracy of both methods. Nonetheless, the interactive method is not as strongly affected, still showing a better precision with a maximum angular spread of  $7^\circ$  between any two data points.

**Table 5:** Mean and maximum angular difference, as well as angular spread in measurements of dislocation line directions of Figure 10b.

<b>u</b>	Mean angular difference [°]		Max. from mean [°]		Spread [°]	
	Analyt.	Interact.	Analyt.	Interact.	Analyt.	Interact.
1	15	6	21	7	24	11
2	15	7	20	9	22	7
3	8	4	14	5	16	8

In Figure 10c and Table 7 we compare line directions determined by the interactive method and trace analysis. The mean orientations for all segments, taken from all five stereo-pairs (●), show a small deviation ( $\leq 5^\circ$ ) from the segment orientations obtained by trace analysis (○) (first column of Table 7). These values do not vary if we exclude orientations measured on stereo-pairs a,b and/or c,d, showing the robustness of the reconstruction method even at smaller  $\vartheta$ . The data points for the stereo-pair c,e (■) are closest to both the mean interactive and trace analysis values for all segments, as seen in the second and third column of Table 7. Stereo-pair c,e has the largest associated  $\vartheta$ , which seems to improve the accuracy of the method, as compared to the stereo-pairs with smaller  $\vartheta$ . Note that the deviation of  $\mathbf{u}_1$ ,  $\mathbf{u}_2$  and  $\mathbf{u}_3$  from the low indexed planes marked in Figure 10c is correctly reproduced by both the mean values and the data point c,e.

Also note that the aspect ratio between the length of the segments (150–200 nm

long, Figure 10d) and the width of the dislocation contrast ( $\approx 4$  nm) is  $\approx 40$ –50. Tracing shorter or curved segments could gradually lead to larger uncertainties in the orientation measurement, although these factors have not been evaluated here. A correct automatic recognition of the segment centerline should nonetheless reduce uncertainties due to manual tracing. Nevertheless, such automatic tracings could be challenging in cases where only residual or double contrast is present (Figures 9a and b), which can be still captured correctly following the present procedure.

**Table 6:** Mean and maximum angular difference, as well as angular spread in measurements of dislocation line directions of Figure 10b, excluding measurements a,b and c,d.

<b>u</b>	Mean angular difference [°]		Max. from mean [°]		Spread [°]	
	Analyt.	Interact.	Analyt.	Interact.	Analyt.	Interact.
1	11	5	16	7	16	7
2	11	6	14	8	17	7
3	10	4	14	5	14	5

**Table 7:** Difference between orientations determined by interactive and trace analysis.

<b>u</b>	Mean vs. trace [°]	c,e (max. 9) vs. mean [°]	c,e (max. 9) vs. trace [°]
1	4	4	2
2	5	5	1
3	3	4	3

The plot in Figure 10d shows the line segment lengths  $|u_1|$ ,  $|u_2|$  and  $|u_3|$ , as obtained by the interactive reconstruction (filled symbols) and the analytical (empty symbols) method. The quantities given in Table 8 show the standard deviation, the maximum deviation from the mean, and the maximum separation between any two measured dislocation line lengths (spread) for the three segments, considering all five stereo-pairs in Figure 9. Regardless of the way of measuring the uncertainties in Table 8, compared to the analytical method, the interactive method shows better precision except for segment 3. The latter systematically shows the largest uncertainty. Agudo Jácome et al. [8] described that diffraction contrast is lost towards one of the surfaces in DFSTEM under these imaging conditions. Because  $u_3$  is the only segment that touches this foil surface, it is also the only segment with a fading contrast towards its end. This fading contrast could lead to different interpretations of where  $u_3$  ends at the surface, depending on the tilt condition. Therefore, it is expected that  $|u_3|$  shows a larger uncertainty, which would also be amplified by short relative displacements at

small stereo-angles. This is in line with the fact that the data points a,b ( $\blacktriangleright$ ) and c,d ( $\blacktriangleleft$ ) fall outside of the cluster of data points for which  $\vartheta > 36^\circ$ , resulting in a spread of 43 nm (see gray arrows in Figure 10d). In a similar manner to what was shown for line orientations in Figure 10b, the analytically determined data points from stereo-pair c,d ( $\blacktriangleleft$ , with the shortest  $\vartheta_{c,d} = 12^\circ$ ) again fall at the outer extremes of their corresponding data sets for  $\langle \mathbf{u}_1 \rangle$  and  $\langle \mathbf{u}_2 \rangle$  in Figure 10d (see two white arrows). Thus, if we include data points a,b and c,d, the mean line lengths and standard deviations are measured as  $\langle \mathbf{u}_1 \rangle = 149 \pm 10$ ,  $\langle \mathbf{u}_2 \rangle = 180 \pm 11$  and  $\langle \mathbf{u}_3 \rangle = 203 \pm 17$  for the interactive and as  $\langle \mathbf{u}_1 \rangle = 147 \pm 19$ ,  $\langle \mathbf{u}_2 \rangle = 194 \pm 18$  and  $\langle \mathbf{u}_3 \rangle = 198 \pm 18$  for the analytical method. The aforementioned errors for the interactive method ( $\approx 8\%$ ) could also be affected by measuring different portions of the short connecting curved segments between segments 1, 2 and 3 (see Figure 9). Note that the accuracy is even improved by adding the measured lengths of all three straight segments  $\langle \mathbf{u}_1 \rangle + \langle \mathbf{u}_2 \rangle + \langle \mathbf{u}_3 \rangle$  (forth row in Table 8), giving an error of  $\approx 2\%$ . Finally, by reconstructing the short curved segments in between and adding them to  $\langle \mathbf{u}_1 \rangle$ ,  $\langle \mathbf{u}_2 \rangle$  and  $\langle \mathbf{u}_3 \rangle$ , we get a total line length  $\langle \mathbf{u} \rangle$ , for which uncertainties are shown in the last row of Table 8. Note that the absolute errors do not vary significantly, yielding a total dislocation line length of  $594 \pm 17$ , which amounts to an error of  $3\%$ . Taking the most conservative measure of error, the spread listed on the last column of Table 8, results in an error of  $7\%$ .

**Table 8:** Standard deviation, maximum difference and spread in measurements of dislocation line lengths of Figure 10d.

$\mathbf{u}$	Standard dev. [nm]		Max. from mean [nm]		Max. separation (spread) [nm]	
	Analyt.	Interact.	Analyt.	Interact.	Analyt.	Interact.
1	19	10	17	12	43	28
2	18	11	28	16	49	30
3	18	17	20	17	40	43
1+2+3	14	10	22	14	36	24
all	-	17	-	17	-	40

If we consider the fact that data points with the smallest  $\vartheta$  seem to systematically affect the accuracy of the measurements, we see a general improvement. Table 9 lists the same quantities as in Table 8, but only considering the three stereo-pairs with  $\vartheta_{1,2} > 36^\circ$ . Thus, the spread for  $\langle \mathbf{u}_3 \rangle$  is reduced from 43 to 15 nm, probably due to a

milder effect of the position set for the diffuse dislocation end at the surface contact. The shorter aspect ratio of  $\|u_1\|$  may be responsible for the large spread (28 nm) kept, but it is clear that the accuracy of the total length  $\|u\|$  of  $605 \pm 8$  nm is still improved to 1.3 %, or 2.5 % if we take the spread (15 nm) as reference.

**Table 9:** Standard deviation, maximum difference and spread in measurements of dislocation line lengths of Figure 10d for  $\vartheta_{1,2} > 36^\circ$ .

<b>u</b>	Standard dev. [nm]		Max. from mean [nm]		Max. separation (spread) [nm]	
	Analyt.	Interact.	Analyt.	Interact.	Analyt.	Interact.
1	15	14	17	12	29	28
2	10	10	2	5	19	19
3	22	8	15	7	40	15
1+2+3	19	7	22	8	36	15
all	-	3	-	17	-	15

## 4. Discussion

### 4.1. Possible Artifacts

Once a node has been manually traced on the left image, the interactive method presented here relies on adjusting the value of  $Z$  in order to match the corresponding position of the node on the right image. In the present implementation, this can be done by directly assigning a  $Z$  value to the node. However, the keyboard arrows or mouse wheel can be alternatively used to change  $Z$  by coarse regular increments (of 5 nm). A selection of several nodes can also be simultaneously moved along  $Z$ . If the parallax is too small (due to, e.g., a small  $\vartheta$ , a segment close to the  $XY$  plane or a short segment), coarse increments in  $Z$ , the simultaneous movement of nodes or a combination of both operations combined can result in segments, for which the parallax was effectively not correctly adjusted. Figure 11a shows a cluster of vertices parallel to the  $XY$  plane that arose in this manner. The plot of azimuth  $\varphi$  vs. polar  $\theta$  angle in Figure 11b shows the same clustering of line directions at the polar angle  $\theta = 90^\circ$ , which is a strong evidence of untouched or simultaneously shifted vertices during the manual depth specification using the interactive reconstruction method of a stereo-pair with a small  $\vartheta$ . These artifacts can be avoided by careful inspection of the  $Z$  values for each affected node. We are currently working on a way to extend the method by vertex, which automatically induces an independent placement of nodes on



both images, to more general tilt scenarios (see Section 6).

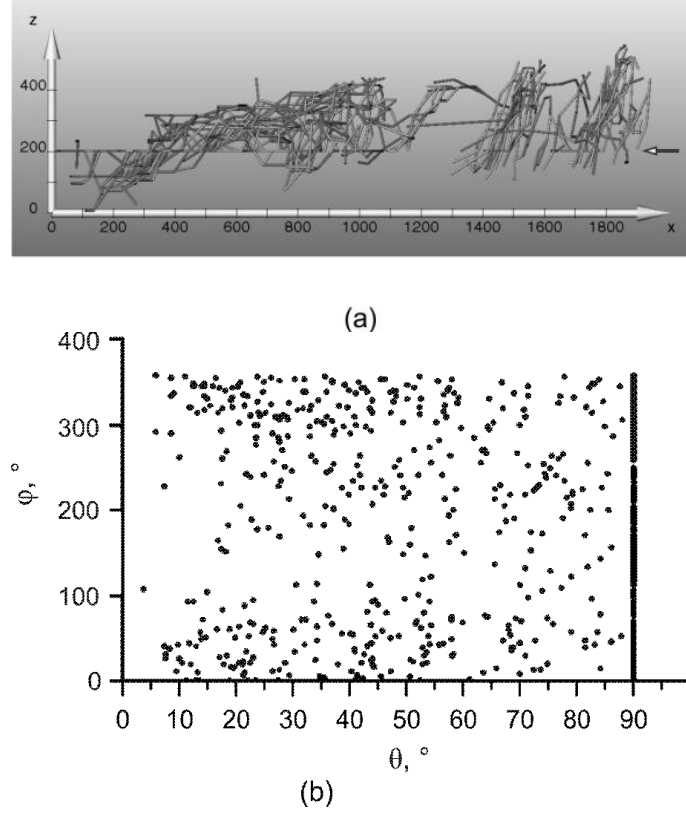


**Figure 11:** Line directions accumulated parallel to  $XY$  plane as shown by (a) spatial graph and (b) scatter plot (azimuthal angle  $\phi$  vs. polar angle  $\theta$ ) of the dislocation line orientations in (a). Notice the accumulation at  $\theta = 90^\circ$ .

#### 4.2. Comparison with Other Methods

Like any method working with stereo-images, our approach can reach only limited accuracy in the case of projections that are horizontal ( $XZ$  plane) in the images. In this case, only the depth positions for the endpoints can be inferred from the parallax but the exact shape of the line (depth positions for all points along the line) cannot be precisely determined. We found only a small number of lines in our experiments running exactly horizontal, which we reconstructed as linear connections between both endpoints. Nevertheless, these horizontal lines could be assessed if additional information on its shape were obtained, e.g., by imaging with other diffraction vectors. For example, the straightness of segments 1, 2 and 3 was verified using the tilt series.

Overall, the results from Figure 10 and Tables 5 to 9 show that accurate

reconstructions can be created. However, the manual tracing can be time consuming. The completion of the reconstructions shown in Figures 6 and 11 took about 5 and 4 hours, respectively, regardless of the tracing approach used. Nonetheless, a quantitative evaluation of foil thickness, dislocation line lengths and directions by traditional methods [e.g. 5,7,26] requires longer and lacks the practical and didactic added value of the reconstructed 3D model. The latter could be imported by modeling tools for use in, e.g., dynamic dislocation simulations, similar to what has been done from other experimental techniques [40]. Likewise, obtaining such experimental 3D models via other techniques such as electron tomography often implies controlling a series of experimental and post-processing parameters [34] that are not needed for STEM stereoscopy. Already adding the time to prepare an adequate sample; set or find the diffraction condition for a specific region of interest; acquire the tilt series and apply the required post-acquisition image filters for tomographic reconstruction, with no guarantee of success, results more time consuming than the method presented here.

A characteristic of STEM diffraction contrast imaging is the possibility of obtaining clear dislocation contrast in multi-beam conditions [35,41,42]. By evaluating stereo-pairs of low indexed zone axes, the possibility to overcome the drawback of dislocations fulfilling the invisibility criterion and simultaneously having a large  $\vartheta$  would have a useful application for accurate dislocation density measurements. Additionally, the uncertainty related with faint contrast towards one of the foil surfaces observed here could be corrected by working in the bright field (BF) mode. These experimental setups will be shown in a separate contribution.

## 5. Conclusions

The viability of reconstructing 3D dislocation arrangements from STEM stereo-pairs has been assessed. For this purpose, a tool, which allows reconstructing, visualizing, manipulating and quantifying dislocation lines –or any linear substructure– by manual tracing of dislocations from stereo-pairs has been implemented for the data analysis framework Amira. Two workflows have been evaluated for the parallax determination, and their advantages and disadvantages have been discussed. While in the past a stereogram was a helpful feature to use stereologic methods for dislocation quantification, it has been shown here that the required small

stereo-angle ( $\approx 8-20^\circ$ ) for appropriate 3D observation can increase the uncertainty of depth measurements. On the other hand, the approach presented here allows lengths and angles to be directly read off with uncertainties of up to 3 % and  $7^\circ$ , respectively, by using larger stereo-angles.

## Outlook

Although we present the feasibility and advantages of manual dislocation substructure reconstructions, efforts in evolving the approach presented here for more accurate and faster reconstructions are needed. Thus, the reconstruction from independent positions of the same feature as performed with the method by vertex could be used in an extension to account for general tilt scenarios, which are commonly found in practice, as shown for the interactive method. To this end, the image setup for the method by vertex could adopt that of the interactive method and calculation of  $Z$  could be made as follows. Figure 12 shows a more detailed version of Figure 2, where fixed known quantities and new variables are defined. The coordinate  $Z_R$  can be defined as  $Z_R = (w_R \cdot \cos \vartheta + T_R) \cdot \sin \vartheta$ , where  $T_R$  is the distance along the direction  $\hat{e}_{T_R}$ , which is contained within the plane of the right image and the model space plane  $XZ$ . The depth difference  $h_R$ , between points  $P_R$  and  $P$ , is related to the horizontal parallax as  $h_R = \Delta X \cdot \cot \vartheta$ . Thus, the depth  $Z = Z_L$  of point  $P$  with respect to the world space can be found as

$$Z = (w_R \cdot \cos \vartheta + T_R) \cdot \sin \vartheta + (X_R - X_L) \cdot \cot \vartheta \quad (1).$$

It is important to keep the correct signs of the quantities  $T_R$ ,  $X_R$  and  $X_L$  in Equation 1, which is why they have been marked as vectors in Figure 12 (and in Figures 2 and 4).

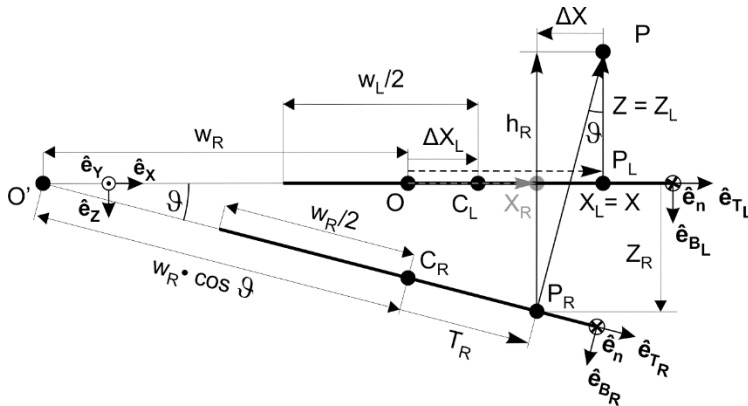


**Figure 12:** Analytical description for future implementation of reconstruction by vertex for the general tilt case by adopting the geometry implemented in the current interactive method.

In passing it should be noted that a shift of the left image in  $X$  by a different  $\Delta X_L$  (which can happen during the procedure of annulling  $\Delta Y$ ) would cause the same shift  $\Delta Z$  for every point in the reconstructed volume. A different  $\Delta X_L$  would shift  $X_L = X$  towards a hypothetical  $X'_L = X'$ , i.e.,  $\Delta X_L = X'_L - X_L$ . Then the new parallax becomes  $\Delta X' = X_R - X'_L = \Delta X - \Delta X_L$ . The associated depth shift  $Z'$  becomes  $\Delta Z = Z' - Z = (\Delta X - \Delta X_L) \cdot \cot \vartheta - \Delta X \cdot \cot \vartheta = \cot \vartheta \cdot (-\Delta X_L)$ . Thus, the same shift in  $X$  seen by every point, induces the same resulting relative depth displacement for every point, i.e.,  $\Delta Z$  is independent of the original position of the point, so that all points see the same  $\Delta X$  and  $\Delta Z$ . Because the main interest lies in the relative positions of points between each other within the sample and not how they are displaced with respect to the world space, the original relative position between the left and right images is irrelevant if  $\Delta Y$  is always zero.

The dislocation contrast obtained in the scanning electron microscopy mode has been exploited here, as it shows a promising potential for semiautomatic or automatic segmentation and reconstruction of lines from stereo-pairs. Therefore, an interesting area for future work is the development of automatic reconstruction methods for 3D lines from STEM stereo-pairs by using similar post-acquisition image filters as in electron tomography, thus allowing the automatic tracing and segmentation of dislocation lines. The advantage would be that the correct image filtering would be needed for only two images with very similar diffraction contrasts, as convenient tilt positions on the diffraction can be chosen, contrary to, e.g., electron tomography. In this sense, the method by vertex serves as the base for calculating the depth positions, once the vertices are previously extracted from the images. Even once automatic methods become available in the future, tools for interactive editing will still be required, for it is to be expected that reconstruction errors occur (due to ambiguities such as crossing lines), making manual corrections necessary. For addressing the problem of lines parallel to the tilt plane, we will additionally consider the possibility of obtaining information from further tilts with the same objects imaged using a different tilt axis.

## Acknowledgements

LAJ acknowledges funding by the German Research Association (DFG) [grant number AG 191/1] and thanks fruitful discussions with Antonin Dlouhý. LAJ and KP acknowledge funding from BAM for performing this research.

## References

- [1] M. von Heimendahl, Specimen thickness determination in TEM in the general case, *Micron*. 4 (1973) 111–116.
- [2] J.W. Edington, *Practical electron microscopy in materials science*, Van Nostrand Reinhold Co., 1976.
- [3] H. Loretto, R.E. Smallman, *Defect Analysis in Electron Microscopy*, Chapman and Hall, 1975.
- [4] R. Ramirez-Mitchell, E.M.B. Sorensen, CTEM versus STEM versus HVEM: Evaluation of the three-dimensional morphology of arsenic inclusions, *J. Electron Microsc. Tech.* 2 (1985) 563–568. doi:10.1002/jemt.1060020606.
- [5] A. Dlouhý, J. Pesicka, Estimate of Foil Thickness by Stereomicroscopy Technique, *Czechoslov. J. Phys.* 40 (1990) 539–555. doi:10.1007/BF01599778.
- [6] D.B. Williams, C.B. Carter, *Transmission Electron Microscopy: A Textbook for Materials Science*, Springer US, 2013.
- [7] A. Dlouhy, G. Eggeler, Superdislocation Line Directions in gamma'-Particles after Double Shear Creep of Superalloy Single Crystals, *Prakt. Met.* 33 (1996) 629–642.
- [8] L. Agudo Jácome, G. Eggeler, A. Dlouhý, Advanced scanning transmission stereo electron microscopy of structural and functional engineering materials, *Ultramicroscopy*. 122 (2012) 48–59. doi:10.1016/j.ultramic.2012.06.017.
- [9] O. Vingsbo, A stereo method for specimen thickness determination in transmission electron microscopy, in: P. Favard (Ed.), *Proc. 7th Int. Congr. Electron Microsc. Société Fr. Microsc. Électronique*, Paris, 1970: pp. 325–326.
- [10] H.J. Klaar, P. Schwaab, W. Österle, Round Robin Investigation into the Quantitative Measurement of Dislocation Density in the Electron Microscope, *Prakt. Met.* 29 (1992) 1–25.
- [11] J. Pešička, A. Aghajani, C. Somsen, A. Hartmaier, G. Eggeler, How dislocation substructures evolve during long-term creep of a 12% Cr tempered martensitic ferritic steel, *Scr. Mater.* 62 (2010) 353–356. doi:10.1016/j.scriptamat.2009.10.037.
- [12] T. Simon, A. Kroeger, C. Somsen, A. Dlouhy, G. Eggeler, On the multiplication of dislocations during martensitic transformations in NiTi shape memory alloys, *ACTA Mater.* 58 (2010) 1850–1860. doi:10.1016/j.actamat.2009.11.028.
- [13] A. Dominguez-Rodriguez, K.P.D. Lagerlöf, A.H. Heuer, Plastic Deformation and Solid-Solution Hardening of, *J. Am. Ceram. Soc.* 69 (1986) 281–284.
- [14] T.M. Pollock, A.S. Argon, Creep resistance of CMSX-3 nickel base superalloy single crystals, *Acta Metall. Mater.* 40 (1992) 1–30. doi:http://dx.doi.org/10.1016/0956-7151(92)90195-K.
- [15] B. Viguier, K.J. Hemker, J. Bonneville, F. Louchet, J.-L.J.-L. Martin, Modelling the flow stress anomaly in  $\gamma$ -TiAl I. Experimental observations of

- dislocation mechanisms, *Philos. Mag. A.* 71 (1995) 1295–1312.  
doi:10.1080/01418619508244375.
- [16] P.B. Hirsch, A. Howie, *Electron Microscopy of Thin Crystals*, Butterworths, London, 1971.
  - [17] G.R. Booker, D.C. Joy, J.P. Spencer, C.J. Humphreys, Imaging of Crystal Defects in the SEM, in: O. Johari (Ed.), *Proc. Work. Electron Specim. Interact. Theory SEM*, IIT Research Institute, Chicago, 1973: pp. 251–258.
  - [18] G.R. Booker, D.C. Joy, J.P. Spencer, H. Graf von Harrach, M.N. Thompson, Contrast Effects from Crystalline Materials Using the Scanning Transmission Electron Microscope (STEM), in: O. Ohari, I. Corving (Eds.), *Proc. 7th Annu. Scanning Microsc. Symp.*, IIT Research Institute, Chicago, 1974: pp. 225–233.
  - [19] T. Yamamoto, H. Nishizawa, Imaging of crystalline substances in scanning transmission electron microscopy, *Phys. Status Solidi.* 237 (1975).  
doi:10.1002/pssa.2210280127.
  - [20] D.M. Maher, D.C. Joy, The Formation and Interpretation of Defect Images from Crystalline Materials in a Scanning Transmission Electron Microscope, *Ultramicroscopy.* 1 (1976) 239–253.
  - [21] P.J. Phillips, M.C. Brandes, M.J. Mills, M. de Graef, Diffraction contrast STEM of dislocations: Imaging and simulations, *Ultramicroscopy.* 111 (2011) 1483–1487. doi:10.1016/j.ultramicro.2011.07.001.
  - [22] J.M. Cowley, Y. Huang, De-channelling contrast in annular dark-field STEM, *Ultramicroscopy.* 40 (1992) 171–180. doi:10.1016/0304-3991(92)90058-R.
  - [23] D.D. Perovic, C.J. Rossouw, a. Howie, Imaging elastic strains in high-angle annular dark field scanning transmission electron microscopy, *Ultramicroscopy.* 52 (1993) 353–359. doi:10.1016/0304-3991(93)90046-Z.
  - [24] Z.L. Wang, Dynamical theories of dark-field imaging using diffusely scattered electrons in STEM and TEM, *Acta Crystallogr. Sect. A Found. Crystallogr.* 51 (1995) 569–585. doi:10.1107/S0108767395002066.
  - [25] J.E. Bailey, P.B. Hirsch, The dislocation distribution, flow stress, and stored energy in cold-worked polycrystalline silver, *Philos. Mag.* 5 (1960) 485–497. doi:10.1080/14786436008238300.
  - [26] R.K. Ham, P. Taylor, R.K. Ham, The determination of dislocation densities in thin films, *Philos. Mag.* 6 (1961) 1183–1184.  
doi:10.1080/14786436108239679.
  - [27] L. Agudo Jácome, P. Nörtershäuser, C. Somsen, A. Dlouhý, G. Eggeler, On the nature of  $\gamma'$  phase cutting and its effect on high temperature and low stress creep anisotropy of Ni-base single crystal superalloys, *Acta Mater.* 69 (2014) 246–264. doi:10.1016/j.actamat.2014.01.021.
  - [28] R.J. McCabe, A. Misra, T.E. Mitchell, K.B. Alexander, A Single-Tilt TEM Stereomicroscopy Technique for Crystalline Materials, *Microsc. Microanal.* 9 (2003) 29–35. doi:10.1017/S1431927603030071.
  - [29] M. Marko, A. Leith, D. Parsons, Three-dimensional reconstruction of cells from serial sections and whole- cell mounts using multilevel contouring of stereo micrographs, *J. Electron Microsc. Tech.* 9 (1988) 395–411.  
doi:10.1002/jemt.1060090406.
  - [30] D. Stalling, M. Westerhoff, H.-C. Hege, Amira: A Highly Interactive System for Visual Data Analysis, in: C.D. Hansen, C.R. Johnson (Eds.), *Vis. Handb.*, Elsevier, Burlington, 2005: pp. 749–767.
  - [31] J.S. Barnard, J. Sharp, J.R. Tong, P. a Midgley, High-resolution three-dimensional imaging of dislocations., *Science.* 313 (2006) 319.

- doi:10.1126/science.1125783.
- [32] J.H. Sharp, J.S. Barnard, K. Kaneko, K. Higashida, P. a Midgley, Dislocation tomography made easy: a reconstruction from ADF STEM images obtained using automated image shift correction, *J. Phys. Conf. Ser.* 126 (2008) 12013. doi:10.1088/1742-6596/126/1/012013.
  - [33] S. Hata, H. Miyazaki, S. Miyazaki, M. Mitsuhashi, M. Tanaka, K. Kaneko, K. Higashida, K. Ikeda, High-angle triple-axis specimen holder for three-dimensional diffraction contrast imaging in transmission electron microscopy, *Ultramicroscopy*. 111 (2011) 1168–1175. doi:10.1016/j.ultramic.2011.03.021.
  - [34] J. Sharp, *Electron Tomography of Defects*, University of Cambridge, 2010.
  - [35] H.K.D.H. Bhadeshia, *Worked Examples in the Geometry of Crystals*, 2nd ed., The Institute of Metals, London, 2001.
  - [36] V.J. Dercksen, H.-C. Hege, M. Oberlaender, The Filament Editor: An Interactive Software Environment for Visualization, Proof-Editing and Analysis of 3D Neuron Morphology, *Neuroinformatics*. 12 (2014) 325–339.
  - [37] L. Agudo Jácome, P. Nörtershäuser, J.-K. Heyer, A. Lahni, J. Frenzel, A. Dlouhy, C. Somsen, G. Eggeler, High-temperature and low-stress creep anisotropy of single-crystal superalloys, *Acta Mater.* 61 (2013) 2926–2943. doi:10.1016/j.actamat.2013.01.052.
  - [38] L. Agudo Jácome, P. Nörtershäuser, C. Somsen, A. Dlouhy, G. Eggeler, On the nature of  $\gamma'$  phase cutting and its effect on high temperature and low stress creep anisotropy of Ni-base single crystal superalloys, *Acta Mater.* 69 (2014) 246–264. doi:10.1016/j.actamat.2014.01.021.
  - [39] A. Prakash, J. Guérolé, J. Wang, J. Müller, E. Spiecker, M.J. Mills, I. Povstugar, P. Choi, D. Raabe, E. Bitzek, Atom probe informed simulations of dislocation-precipitate interactions reveal the importance of local interface curvature, *Acta Mater.* 92 (2015) 33–45. doi:10.1016/j.actamat.2015.03.050.
  - [40] L.A. Jácome, C. Somsen, G. Eggeler, Systematic dislocation analysis assessment by HAADF STEM imaging, *MC 2009, Vol 3 Mater. Sci.* 3 (2009) 201–202. doi:10.3217/978-3-85125-062-6-473.
  - [41] P.J. Phillips, M.J. Mills, M. De Graef, Systematic row and zone axis STEM defect image simulations, *Philos. Mag.* 91 (2011) 2081–2101. doi:10.1080/14786435.2010.547526.